THE JOURNAL OF PHYSICAL CHEMISTRY B

B: Fluid Interfaces, Colloids, Polymers, Soft Matter, Surfactants, and Glassy Materials

Ion-specific Confined Water Dynamics in Convex Nanopores of Gemini Surfactant Lyotropic Liquid Crystals

Grayson L. Jackson, Sriteja Mantha, Sung A Kim, Souleymane O Diallo, Kenneth W. Herwig, Arun Yethiraj, and Mahesh K. Mahanthappa

J. Phys. Chem. B, **Just Accepted Manuscript** • DOI: 10.1021/acs.jpcb.8b05942 • Publication Date (Web): 25 Sep 2018

ACS Publications

is published by the American Chemical Society. 1155 Sixteenth Street N.W., Washington, DC 20036

Ion-specific Confined Water Dynamics in Convex Nanopores of Gemini Surfactant Lyotropic Liquid Crystals

Grayson L. Jackson,[†] Sriteja Mantha,[†] Sung A Kim,[‡] Souleymane O. Diallo,[§] Kenneth W. Herwig,[#] Arun Yethiraj,[†] and Mahesh K. Mahanthappa[†,‡,*]

[†]*Department of Chemistry, University of Wisconsin–Madison, 1101 University Ave., Madison, WI 53706*

[§]*Chemical and Engineering Materials Division, Oak Ridge National Laboratory, Oak Ridge, TN 37831 USA*

[#]*Neutron Scattering Science Division, Oak Ridge National Laboratory, Oak Ridge, Tennessee 37831, USA*

[‡] *Department of Chemical Engineering & Materials Science, University of Minnesota, 421 Washington Ave, S.E., Minneapolis, MN 55455*

ABSTRACT

The impact of pore geometry and functionality on the dynamics of water nanoconfined in porous media are the subject of some debate. We report the synthesis and small-angle X-ray scattering (SAXS) characterization of a series of perdeuterated gemini surfactant lyotropic liquid crystals (LLCs), in which convex, water-filled nanopores of well-defined dimensions are lined with carboxylate functionalities. Quasielastic neutron scattering (QENS) measurements of the translational water dynamics in these dicarboxylate LLC nanopores as functions of the surfactant hydration state and the charge compensating counterion (Na^+, K^+, NMe_4^+) reveal that the measured dynamics depend primarily on surfactant hydration, with an unexpected counterion dependence that varies with hydration number. We rationalize these trends in terms of a balance between counterion-water attractions and the nanopore volume excluded by the counterions. On the basis of electron density maps derived from SAXS analyses of these LLCs, we directly show that the volume excluded by the counterions depends on both their size and spatial distribution in the water-filled channels. The translational water dynamics in the convex pores of these LLCs are also slower than those reported in the concave pores of AOT reverse micelles, implying that water dynamics also depend on the nanopore curvature.

INTRODUCTION

Nanoconfined water exhibits unusual properties,[1] since the presence of an interface disrupts the structure[2-4] of its hydrogen bonding network and perturbs its dynamics.[5-7] Confined water dynamics profoundly influence biomolecule function,[8-10] mesoporous inorganic catalyst performance,[11] and water and ion transport through porous polymer membranes.[12, 13] In order to better understand these phenomena, water dynamics have been investigated in model systems such as the concave nanopools formed by reverse spherical micelles (RMs)[14-16] or at planar lipid bilayer interfaces.[17] However, recent experiments and related simulations suggest that water rotational dynamics in convex pores are faster than in concave ones,[7, 18] albeit with some disagreement regarding the magnitude of these effects. Simulations of protein hydration shells[19, 20] and experiments on water confined in concentrated protein solutions[21, 22] also indicate that water dynamics depend sensitively upon surface chemical functionalities and topologies. Thus, a fundamental understanding of nanoconfined water dynamics at convex, functional interfaces is important and may guide the design of next-generation ion transporting membranes.[23]

A molecular-level understanding of the factors governing nanoconfined water dynamics requires a well-defined model system with tunable pore sizes, interfacial curvatures, and pore chemical functionalities. Formed by water concentration-dependent ionic amphiphile self-assembly, lyotropic liquid crystals (LLCs) are an attractive platform for studying water dynamics within monodisperse, convex nanopores with tunable diameters $d \approx 0.7$-4 nm (Figure 1).[7, 24, 25] The surfactant headgroup and charge compensating counterion specify the interfacial chemical functionalities, while the nanopore diameter and geometry may be tailored by modifying the headgroup hydration state or amphiphile structure. LLCs exhibit a variety of ordered phases with different mean interfacial curvatures, including lamellae (L_α), hexagonally-packed cylinders (H),

and bicontinuous network phases. Network phase LLCs are particularly sought after for selective ion transport[26] and water purification[27] applications due to their interpenetrating and percolating aqueous and hydrocarbon nanodomains. As shown by Gin[28] and Mahanthappa,[29,30] gemini ("twin tail–twin head") amphiphiles enable robust access to network phase LLCs such as the double gyroid (G_I) morphology (Figure 1).

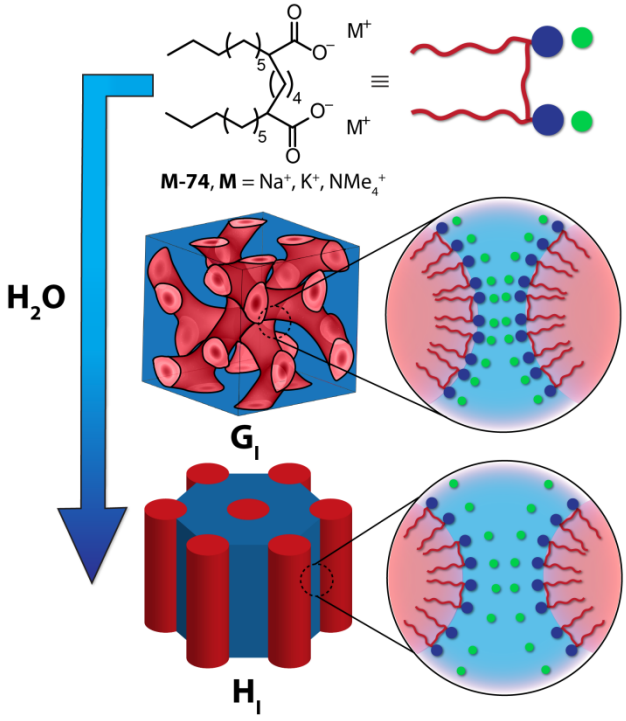

Figure 1. Water-driven self-assembly of gemini dicarboxylate amphiphiles affords well-defined convex nanochannels lined with carboxylate functionalities and filled with hydrated surfactant counterions. Gemini amphiphiles form bicontinuous double gyroid network (G_I) phases at low hydrations and hexagonally-packed cylinders (H_I) at higher hydrations.

Previous experimental studies and computer simulations of LLCs have provided initial insights into how pore geometry and interfacial chemical functionalities affect nanoconfined water

dynamics therein. A combination of 2D–IR spectroscopy and molecular dynamics (MD) simulations indicated that water rotational dynamics in the convex pores of a G_I phase of a disodium dicarboxylate gemini amphiphile (Figure 1) were faster than those in concave sodium sulfonate-lined **Na-AOT** RMs with similar confinement diameters $d \sim 15$ Å.[7] However, the more delocalized charge density of the sulfonate headgroups would lead one to anticipate weaker water-headgroup interactions[31] and faster water dynamics. Thus, this study suggests that the effects of nanopore curvature may outweigh those of pore chemistry. In order to systematically isolate the effects of confinement diameter, interfacial curvature, and interfacial chemistry, McDaniel *et al*.[18] compared MD simulations of disodium dicarboxylate and disodium bis(sulfonate) gemini surfactant LLCs at identical headgroup hydrations to elucidate differences in water dynamics in $d \sim 10$ Å pores. Their studies highlight the subtle interplay between the size of a headgroup (pore) functionality and its short-range interactions with water molecules, which influence the rotational and translational dynamics of water in different ways. However, this study neglects any effects arising from molecular-level details such as the substantial differences in headgroup-counterion pairing for sodium carboxylates *versus* sodium sulfonates,[32, 33] and the counterion distributions within the aqueous channels.

In this report, we describe combined small-angle X-ray scattering (SAXS) and quasielastic neutron scattering (QENS) studies of nanoconfined water dynamics within the convex pores of alkyl dicarboxylate gemini surfactant LLCs. To minimize the incoherent scattering signal from the surfactant matrix in the QENS measurements, we synthesized new perdeuterated gemini surfactants that were hydrated with H_2O to yield perdeuterated gemini dicarboxylate LLCs with various counterions, designated **Na-74d**, **K-74d**, and **NMe_4-74d** (Figure 1). By experimentally measuring the dynamic structure factor $S(q,E)$ of H_2O in these selectively deuterated LLCs as a

function of the momentum transfer vector q by QENS, we determine the LLC water self-diffusion coefficients as functions of overall hydration and ionic surfactant counterion. We observe that water diffusivity depends most sensitively on hydration: the dynamics are faster with increasing hydration. We also find marked changes in water self-diffusion depending on the identity of the surfactant counterion (Na^+, K^+, NMe_4^+), including counterintuitive variations with surfactant hydration. These results favorably compare with recently published MD simulations on exactly these systems,[34] which provide a basis for rationalizing the experimentally-observed trends. The MD simulations suggest that these trends reflect a competitive balance between counterion-water attractions and counterion size-dependent excluded volume in the aqueous nanochannels, while neglecting entirely the roles of cation-headgroup pairing or the cation distribution in the channels. While counterion excluded volume in a nanopore depends on its size, we use SAXS-derived electron density maps for the perdeuterated LLCs to demonstrate directly that the spatial distribution of counterions in the nanochannels also impacts their excluded volume. Consequently, we revise the physical picture previously presented by Mantha *et al*.[34] to incorporate the unrecognized role of counterion distribution on the water dynamics in the ionic nanochannels of gemini dicarboxylate LLCs. Comparisons of the measured water self-diffusion coefficient in **Na-74d** G_I phases to previously reported QENS studies of **Na-AOT** RMs unexpectedly suggest that convex pores lead to slower water translation than concave nanopores.

EXPERIMENTAL METHODS

Materials and Methods. Decanoic acid–d_{19} (98.7% D) and 1,4-dibromobutane–d_8 (100% D) were purchased from CDN Isotopes (Quebec, Canada). Decanoic acid–d_{19} was used as received and 1,4-dibromobutane–d_8 was distilled, degassed, and stored under nitrogen and away from

light. Tetramethylammonium hydroxide $N(CD_3)_4OD•5D_2O$ (98% D) was purchased from Cambridge Isotopes Laboratories (Cambridge, MA). High-purity D_2O (99.9% D sealed in ampules) and all other materials and reagent grade solvents were purchased from Sigma-Aldrich (Milwaukee, WI), and they were used as received unless noted. Hexamethylphosphoramide (HMPA) and diisopropylamine (HN^iPr_2) were distilled from CaH_2 and stored under nitrogen. Anhydrous and anaerobic tetrahydrofuran (THF) was obtained by purging analytical grade solvent with nitrogen for 30 min followed by cycling through a column of activated alumina for 12 h in a VacATM Solvent Purification System (SPS). *n*-Butyllithium (2.5 M in hexanes) was titrated against diphenylacetic acid in anhydrous and anaerobic THF prior to use. Type I ultra-pure water was obtained from a Thermo Scientific Barnstead NANOpure™ system (18.2 MΩ•cm resistivity) and sparged with $N_2(g)$ prior to use.

^2H and ^{13}C NMR spectra were recorded on either: (1) a Bruker Avance 500 spectrometer with a DCH cryoprobe or (2) a Bruker Avance III HD 500 spectrometer with a TCI cryoprobe. ^2H spectra were recorded in protiated CH_3OH or DMSO and referenced relative to the residual deuterated solvent resonance. ^{13}C spectra were recorded in either DMSO-d_6 or CD_3OD-d_4 and referenced to the solvent peaks. Mass spectrometry was performed using a Waters (Micromass) LCT® electrospray ionization TOF spectrometer operating in negative ion detection mode with a sample cone voltage of 20 V. Infrared spectra were recorded on a Bruker Tensor FTIR between 4000-500 cm^{-1}, using a diamond crystal attenuated total reflectance (ATR) stage. Combustion analyses (C, H, and N) were performed by Atlantic Microlab, Inc. (Norcross, GA, USA).

Perdeuterated Surfactant Syntheses. Perdeuterated gemini dicarboxylate surfactants were synthesized from decanoic acid–d_{19} (98.7% D) and 1,4-dibromobutane–d_8 (100% D) by analogy to a previously reported procedure[29] (see Supporting Information for synthesis details). After

three recrystallizations from EtOH, d_{44}-docosane-9,14-dicarboxylic acid was quantitatively deprotonated using either $Na_2CO_3(s)$, $K_2CO_3(s)$, or $(CD_3)_4NOH(aq.)$ (98% D) to yield **Na-74d**, **K-74d**, or **NMe_4-74d**, respectively. These crystalline powders were azeotropically freeze-dried from C_6H_6. LLC samples used for QENS background subtraction (perdeuterated surfactant in D_2O) were additionally freeze-dried from D_2O to minimize residual H_2O; the extent of this exchange was quantified using ATR-FTIR by ratiometric analysis of the intensities of the O–H and O–D vibrations at 3280 and 2460 cm^{-1}, respectively. Sample purity and residual water content were determined by elemental combustion analysis, where deuterium was analyzed as hydrogen.

Anal. Calc. for **Na-74d**: $C_{24}D_{44}O_4Na_2$•0.67H_2O: C, 57.78; H, 9.16; Found: C, 57.77; H, 9.15. For the background sample freeze-dried from D_2O: *Anal*. Calc.: $C_{24}D_{44}O_4Na_2$•0.16 H_2O•0.66 D_2O: C, 57.31; H, 9.15; Found: C, 57.31; H, 9.18.

Anal. Calc. for **K-74d**: $C_{24}D_{44}O_4K_2$•0.75H_2O: C, 54.12; H, 8.61; Found: C, 54.14; H, 8.75. For the background sample freeze-dried from D_2O: *Anal*. Calc.: $C_{24}D_{44}O_4K_2$•0.23 H_2O•0.87 D_2O: C, 53.31; H, 8.61; Found: C, 53.30; H, 8.72.

Anal. Calc. for **NMe_4-74d**: $C_{32}D_{68}O_4N_2$•2.08H_2O: C, 59.06; H, 11.18; N, 4.31. Found: C, 59.05; H, 10.96; N, 4.36. For the background sample freeze-dried from D_2O: *Anal*. Calc.: $C_{32}D_{68}O_4N_2$•1.1 H_2O•1.7 D_2O: C, 57.56; H, 11.12; N, 4.20. Found: C, 57.57; H, 10.78; N, 4.14.

LLC Sample Preparation. Purified surfactants were massed into 4 dram vials in an argon-filled glovebox. Two sets of QENS samples were then prepared outside of the glovebox for each surfactant and hydration: one in H_2O, and another in D_2O for background subtraction. Accounting for the residual water content of the crystalline surfactants determined from elemental analyses, we added precise amounts of Type I ultrapure H_2O or D_2O to achieve the

desired surfactant hydration numbers w_0 = (total moles water)/(moles $-CO_2^-$ headgroup) = 6 or 15. These components were homogenized using successive cycles of high-speed centrifugation (4996 x *g*) and hand-mixing by spatula. LLC samples were stored in Teflon-capped vials sealed with Parafilm to minimize sample dehydration.

Small-angle X-ray Scattering (SAXS). LLC samples were characterized by laboratory source and synchrotron X-ray scattering. Details of the lab source SAXS analyses used to confirm LLC morphologies prior to QENS measurements are given in Supporting Information. Synchrotron SAXS analyses of **Na-74d**, **K-74d**, and **NMe_4-74d** LLCs with w_0 = 6 and 15 were performed at the 12-ID-B beamline of the Advanced Photon Source (APS) at Argonne National Laboratory (Argonne, IL), using a beam energy of 14.00 keV (λ = 0.8856 Å) and a 2.027 m sample-to-detector distance. 2D–SAXS patterns were recorded on a Pilatus 2M detector with 1475 x 1679 pixel resolution. Samples were sealed in hermetic alodined aluminum DSC pans and were measured at 298 K with a 0.1 s exposure time. All acquired scattering patterns were calibrated against a silver behenate standard (d_{100} = 58.38 Å). The DataSqueeze[35] software package was used to azimuthally-integrate 2D-SAXS patterns to produce one-dimensional I(*q*) *versus q* intensity profiles.

Quasielastic Neutron Scattering (QENS) Data Acquisition and Analysis. LLC samples were loaded into aluminum flat plate cells (3 cm × 5 cm) with a 100 μm gap for QENS measurements. This hydrated sample thickness was selected to ensure ≥ 90% neutron transmission, so that multiple-scattering effects could be neglected. Sample cells were sealed with an indium wire O-ring under 1000 psi hydraulic compression at 25 °C. QENS data were collected on the backscattering spectrometer (BASIS) at the Spallation Neutron Source (SNS) at Oak Ridge National Laboratory (Oak Ridge, TN). In this inverted-geometry neutron

spectrometer, a final neutron wavelength of 6.274 Å set by the analyzer crystals led to an accessible energy transfer to the sample in the range -120 < E < 120 μeV with 0.4 μeV resolution. Data were collected in the range $0.2 \le q \le 2.0$ Å^{-1} and binned into 0.2 Å^{-1} groups. The reported q–values for the QENS spectra correspond to the middle of each of these bins.

Data for each LLC prepared using H_2O were first collected at 298 K and then at 50 K, where proton motion ceases, in order to obtain the sample-dependent instrument resolution function, $R(q,E)$. Background samples prepared using D_2O were only measured at 298 K. Data were typically acquired for 6 h, and measured QENS intensities were normalized to that of a vanadium standard in a similar flat-plate geometry. For **Na-74d** (w_0 = 6 and 15) and **NMe$_4$-74d** (w_0 = 6), we also collected elastic intensity scans in 2 K increments while cooling from 298 K to 236 K and at 200, 170, 140, 100, and 50 K. Sample temperature was controlled within ±1 K with a 2 min thermal equilibration time and ~5 min acquisition time at each temperature.

QENS data reduction and spectral fits employed the Mantid software suite[36, 37] including various custom QENS spectral fitting scripts available at the BASIS beam line. Initial data fits by either a sum of Lorentzian functions or the Fourier transform of a Kohlrausch-Williams-Watts (KWW) stretched exponential function resulted in reasonable $\chi^2 \le 5$. However, the data were best fit by the KWW function that assumes a distribution of water relaxation times in the LLC nanopores (*vide infra*). More explicitly, we used the following fitting model:

$$S(q,E) = \left[A(q)FT\left\{\exp\left[-\left(\frac{t}{\tau(q)}\right)^{\beta}\right] + a(q)\times\delta(E)\right\}\right]\otimes R(q,E) + b_w(q)\times S_{background}(q,E) + C(q) \quad (1)$$

where $S(q,E)$ is the measured QENS spectra for the perdeuterated surfactant LLC with H_2O, and the KWW function pre-factor $A(q)$ is the intensity associated with the quasielastic scattering from H_2O. The weighting function $a(q)$ applied to the elastic scattering $\delta(E)$ stems from three

different contributions: (1) excess elastic intensity not eliminated by the background subtraction process due to differences in the coherent contrast and small-angle neutron scattering (SANS) between the D_2O/perdeuterated surfactant and H_2O/perdeuterated surfactant LLC samples, (2) elastic intensity due to any immobile water H-atoms on the timescale of the instrument resolution function, and (3) q-dependent elastic intensity from the elastic incoherent structure factor, $EISF(q)$, which arise from geometric restrictions to translational diffusion. The scattering signal contributions in square brackets in Eq. (1) are convoluted with the sample-dependent resolution function $R(q,E)$ determined at 50 K. $S_{background}(q,E)$ are the measured background spectra for perdeuterated surfactant LLC samples prepared with D_2O weighted by a scaling term, $b_w(q)$, and $C(q)$ is a linear background.

A sequential fit to Eq. (1) at each q–value was used to determine the initial parameters for a global, simultaneous fit for q = 0.3 Å^{-1}–1.9 Å^{-1}, using the six fitting variables $A(q)$, $\tau(q)$, $\beta(q)$, $a(q)$, $b_w(q)$, and $C(q)$. For the global fit seeded with these values, the value of β was assumed to be independent of q. This last assumption is validated by the observation that the β obtained from a sequential fit at each q is nearly q-independent (see Figure S1). Each set of spectra was globally fit a total of five times using different initial input parameters. Table S1 enumerates representative global fit values from Eq. (1) obtained for each system.

We also performed global, simultaneous fits of the data using Eq. (2), in which both b_w and β are held constant and optimized over the range $0.3 \le q \le 1.3$ Å^{-1}:

$$S(q,E) = \left[A(q)FT\left\{\exp\left[-\left(\frac{t}{\tau(q)}\right)^{\beta}\right] + a(q)\times\delta(E)\right\}\right]\otimes R(q,E) + b_w \times S_{background}(q,E) + C(q) \quad (2)$$

Representative fitting parameter values obtained using Eq. (2) are given in Table S2. The optimized values of b_w approximately correspond to the mass ratio of the H_2O LLC sample to

that of the D_2O background LLC, as expected. The orientation of the flat-plate sample cell with respect to the incoming neutron beam significantly attenuates $S(q,E)$ above q = 1.3 Å^{-1}. Consequently, attempts to perform global, simultaneous fits including data for q > 1.3 Å^{-1} with a q-independent b_w typically gave poor fits, which we ascribe to slight differences in the orientations of the H_2O and D_2O LLC samples in the neutron beam that result in large changes in the relative signal attenuation. The χ^2 values for the fits using Eq. (2) are comparable to those obtained with Eq. (1). We fit each set of spectra a total of four times using Eq. (2), from which we estimate a ±10% relative standard deviation in the obtained self-diffusion coefficients $\langle D \rangle$.

The proton mean-squared displacement ($\langle u_x^2 \rangle$) was also determined using the temperature-dependent elastic intensity taken during fixed window scans. The q-dependence over the range 0.09 Å^{-2} < q^2 < 3.61 Å^{-2} of the elastic intensity was used to extract $\langle u_x^2 \rangle$ by fitting against:

$$\ln\left(\frac{I(q)}{I_o(q)}\right) = -\frac{q^2\langle u^2\rangle}{3} = q^2\langle u_x{}^2\rangle \tag{3}$$

where $I(q)$ is the elastic intensity at a given temperature normalized by the elastic intensity $I_0(q)$ at 50 K.

RESULTS

QENS is a well-established, non-invasive technique for measuring water dynamics in a variety of chemical environments.[16, 24, 38, 39] This incoherent scattering technique measures the broadening in energy transfer (E) around an elastic scattering peak arising from atomic motion, thus providing a direct measure of the dynamic structure factor $S(q,E)$ at various scattering wavevectors (q). $S(q,E)$ contains contributions from translational, rotational, and vibrational dynamics, which can be deconvoluted to reveal translational dynamics information.

QENS is particularly suited for studies of water dynamics in soft materials due to the large incoherent scattering cross-section of ^{1}H as compared to ^{2}H, which enables isolation of the ^{1}H dynamics of interest through selective sample deuteration. Consequently, we sought to specifically study confined $^{1}H_2O$ dynamics within the convex nanopores of LLC materials comprising perdeuterated ionic surfactants hydrated with H_2O. By analogy to the synthetic procedure developed by Sorenson *et al*.[29], we synthesized a perdeuterated gemini dicarboxylic acid from decanoic acid-d_{19} and 1,4-dibromobutane-d_8 (Scheme 1). Subsequent stoichiometric deprotonation with $Na_2CO_3(s)$, $K_2CO_3(s)$, or $(CD_3)_4NOH(aq)$ afforded the analytically pure gemini dicarboxylate amphiphiles **Na-74d**, **K-74d**, and **NMe$_4$-74d**, respectively.

Scheme 1. Syntheses of Perdeuterated Gemini Dicarboxylate Surfactants (**M-74d**)

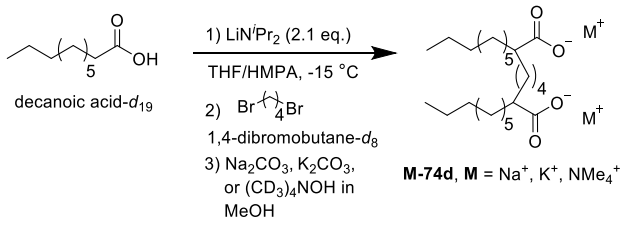

Synchrotron SAXS confirmed that LLC samples formed with w_0 = (total moles water)/(moles $-CO_2^-$ headgroup) = 6 form normal double gyroid (G_I) phases ($Ia\bar{3}d$ symmetry) with cubic unit cell parameters a = 6.7 nm (q^* = 0.94 nm^{-1}) for all three counterions. (Figure 2A) This morphology comprises two interpenetrating hydrophobic 3-fold connector networks in a water matrix as depicted in Figure 1. SAXS analyses of samples with w_0 = 15 reveal the formation of H_I phases (*P6mm* symmetry) with intercylinder center-to-center distances of 4.0 nm (q^* = 1.8 nm^{-1}; Figure 2B) for all counterions. These results concur with those previously reported for the

protiated surfactant analogs,[29] indicating that there is no significant effect of isotopic substitution on the self-assembly behaviors of these amphiphiles.

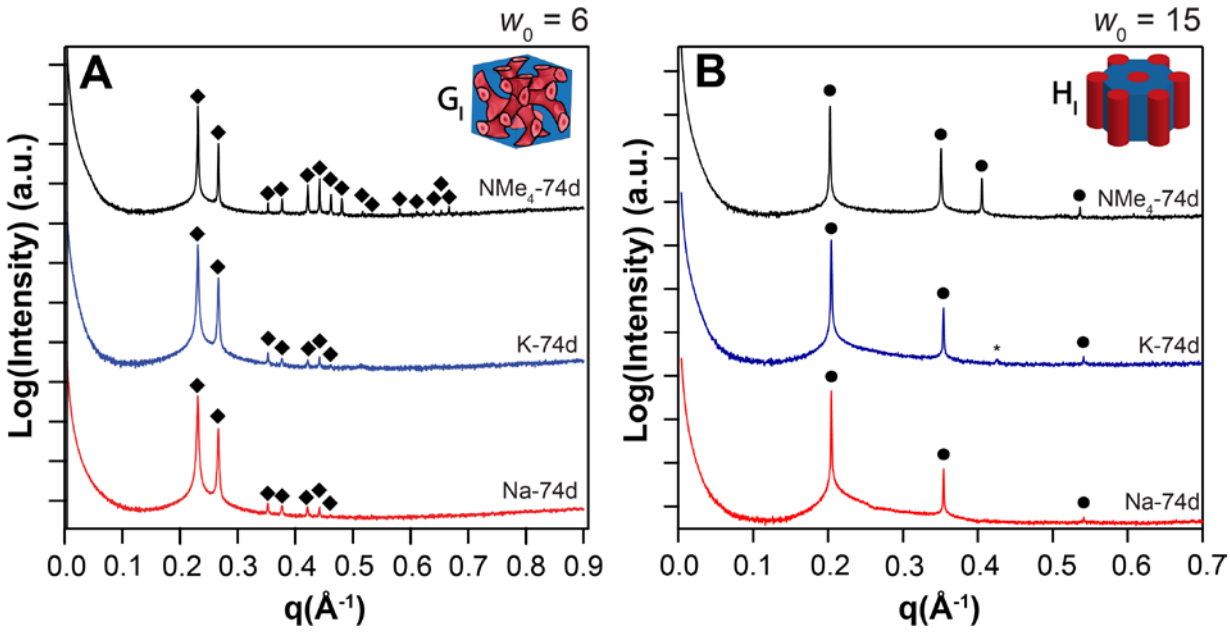

Figure 2. Azimuthally-integrated SAXS profiles for perdeuterated gemini dicarboxylates **Na-74d**, **K-74d**, and **NMe$_4$-74d** formed at (**A**) w_0 = 6 match the expected reflections for a G_I phase (*diamonds*), while those formed at (**B**) w_0 = 15 match the expected reflections for a H_I phase (*circles*). The asterisk (*) denotes an artifact arising from the sample holder.

Figure 3 depicts QENS-based $S(q,E)$ for a **Na-74d** LLC with w_0 = 6 obtained at specific scattering wavevector values (q). Generally, the quasielastic peak broadens and monotonically decreases in intensity as q increases. The anomalously low intensity at q = 1.7 Å^{-1} stems from a scattering artifact from the flat-plate sample geometry at the BASIS spectrometer.

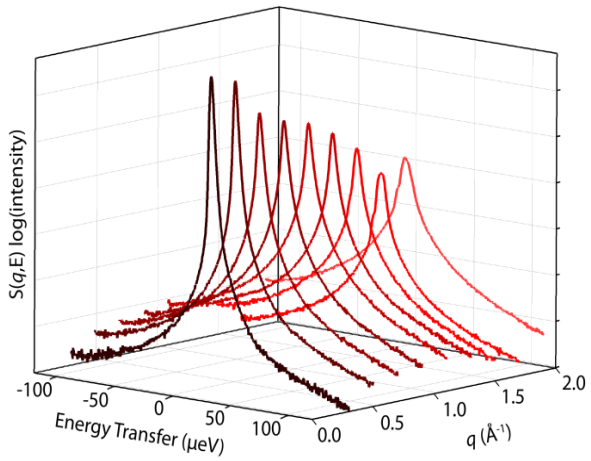

Figure 3. Vanadium-normalized QENS spectra for **Na-74d** showing $S(q,E)$ on a log(intensity) scale versus energy transfer, E, as a function of scattering wave vector, q, at 298 K. We attribute the decreased intensity at q = 1.7 Å^{-1} to an artifact from the flat-plate sample holder.

Note that the experimentally measured $S(q,E)$ contains contributions from: (1) vibrational dynamics that are faster than the instrument resolution, (2) surfactant motions, (3) elastic intensity arising from Bragg scattering (SANS) from the ordered LLC morphology and from any immobile water molecules on the timescale of the instrument resolution, and (4) quasielastic scattering contributions from water dynamics that we seek to analyze in detail (see Experimental Methods section for details). MD simulations by Mantha *et al.*[34] of the systems experimentally considered here indicate that the H_2O residence times are sub-100 ps at $w_0 = 6$. Thus, any water molecules immobile on the timescale of the instrument resolution probably interact strongly with the carboxylate headgroup or counterions, and that fraction of immobile hydration waters increases as w_0 decreases. However, we are unable to quantify the fraction of immobile water molecules due to the non-trivial contributions of SANS to the elastic intensity. In our QENS spectral analyses, a linear background approximating a frequency-independent Debye-Waller factor ($C(q)$ in Equations (1) and (2)) was consequently used to account for these vibrational

dynamics. While contributions from surfactant motion are certainly mitigated by amphiphile deuteration, we further minimized these contributions by a spectral background subtraction with a LLC sample prepared with perdeuterated gemini surfactant in D_2O at the same w_0. Note that previous QENS investigations of water diffusion within perfluorosulfonate LLCs made no attempt to remove such contributions to $S(q,E)$ arising from surfactant dynamics.[40]

QENS contributions due to water motion are typically fit using either a sum of Lorentzian functions or using the Fourier transform of a Kohlraush-Williams-Watts (KWW) stretched exponential function. Mantha and Yethiraj recently used MD trajectories, from which the water self-diffusion coefficients $\langle D \rangle$ were explicitly evaluated, to calculate $S(q, E)$ and to assess the fitting accuracy of these two approaches to $\langle D \rangle$ for water nanoconfined in G_I and H_I gemini dicarboxylate LLCs.[41] While the intermediate scattering function (ISF) was better fit by a KWW function than a sum of Lorentzian functions, they concluded that both fitting approaches yielded $\langle D \rangle$ values that were systematically lower than those calculated directly from the MD trajectories. Although the deviation for the H_I phase was minor, the deviation in $\langle D \rangle$ for the G_I phase was ~15%. Upon fitting our experimental data using both approaches, we found that a KWW function better fit our QENS spectra than a sum of Lorentzian functions (lower χ^2 values).

The KWW function physically describes water translation based on a relaxing cage model (RCM) with two fitting parameters, τ and β.[42, 43] At short timescales in the RCM, a water molecule is trapped by its surrounding solvation shell. Thermal fluctuations structurally relax this cage with a characteristic time τ, allowing the water molecule to escape and enter a new solvent cage. The stretching exponent β serves as an indicator of dynamic heterogeneity, whereby a broader distribution of relaxation times results in smaller β–values. MD simulations of the specific gemini dicarboxylate LLCs considered here[34] revealed large differences in the

residence times of H_2O molecules around headgroups, counterions, and other water molecules. This apparent dynamic heterogeneity bolstered our preference for a KWW function as the most physically reasonable model fit. As detailed in the Experimental Methods section, we utilized a sequential fit of $S(q,E)$ at each q-value to generate initial inputs for a simultaneous (global) $S(q,E)$ fit over all q-values. Overall, the global fits to Equations (1) and (2) are acceptable, with $\chi^2 < 2$ for $w_0 = 6$ and $\chi^2 < 5$ for $w_0 = 15$ (Figure 4; see Tables S1-2 for representative fitting parameters). Note that the $\delta(E)$ apparently does not completely capture all the elastic intensity due to SANS from the ordered LLC structure, resulting in the observed residuals.

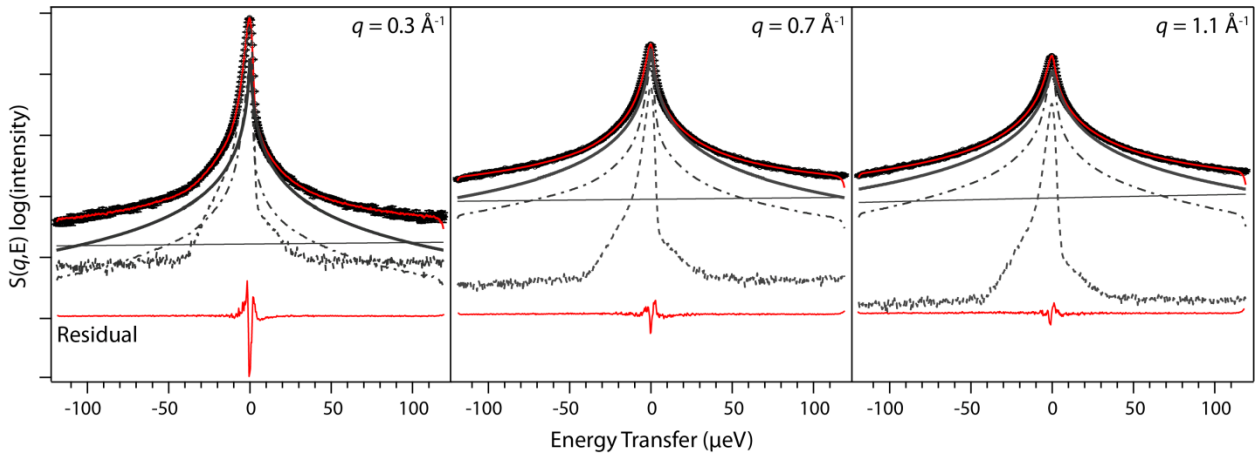

Figure 4. Representative $S(q,E)$ measured by QENS (*black circles with error bars*) and associated global fit from Eq. (1) (*solid red line*) for **Na-74d** at q = 0.3, 0.7, and 1.1 Å^{-1} presented on a log(intensity) scale. The fit contains four terms: a $\delta(E)$–function (*dashed gray line*), a linear background $C(q)$ (*solid straight line*), a fit of the scaled D_2O background $b_w(q)\bullet S_{background}(q,E)$ (*dash-dot gray line*), and a KWW function (*solid gray line*). The linear scale residual at the bottom stems from excess elastic intensity from SANS from the underlying, spatially periodic LLC morphology.

The RCM τ and β parameters from the QENS spectral fits depend on the hydration level and counterion identity. The relaxation time τ decreases as a function of q (Tables S1-2). We ascribe the large increase in τ at low q to increased residual elastic intensity from SANS peaks caused by the periodic LLC morphology. In global fits of the QENS data, we assumed the stretching exponent (β) to be q-independent (Figure S1; see Experimental Methods Section). The value of β

~ 0.75 at w_0 = 15 and decreases to β ~ 0.6 at the lower w_0 = 6, implying increasingly heterogeneous dynamics upon reduction of the confinement (pore) diameter. Previous studies of water confined to inorganic nanocages[38] and nanoporous silica[44] reported comparable β-values that were similarly q-independent. The KWW fitting parameters can be combined to determine an average relaxation time ($<\tau_\beta>$) per Zanotti *et al*.:[45]

$$\left\langle \tau_\beta \right\rangle = \frac{\tau}{\beta}\Gamma\left(\frac{1}{\beta}\right) \tag{4}$$

For the purposes of QENS analyses, one typically assumes a decoupling approximation whereby the ISF can be approximated as the product of the translational ISF and the rotational ISF where the former function dominates at $q \leq 1.0$ Å^{-1}.[46] The decoupling approximation validity has been questioned and more sophisticated models have been developed to include coupling,[43] although Liu *et al*.[47] found the decoupling approximation was accurate for $q \leq 0.75$ Å^{-1} with only ~ 9% deviation at higher q-values. Explicit evaluation of the ISF in MD simulations of water nanoconfined in a **Na-74** G_I phase at w_0 = 6 supports this decoupling approximation, by demonstrating that the signal is dominated by the translational ISF for $q < 1.3$ Å^{-1}.[41] Thus, we focus on data measured between 0.3 Å^{-1} ≤ q ≤ 1.1 Å^{-1} in determining the water self-diffusion coefficients $<D>$.

The $<\tau_\beta>$ corresponding to unrestricted diffusive motion should scale as $1/<\tau_\beta> \sim q^\gamma$, where γ= 2 in the hydrodynamic limit.[38] For all LLCs at w_0 = 15 and **NMe_4-74d** at w_0 = 6, a power–law fit over 0.3 Å^{-1} ≤ q ≤ 1.1 Å^{-1} reveals $\gamma \sim 2$. For both **Na-74d** and **K-74d** at w_0 = 6, $\gamma \sim$ 2.4–2.8 . The latter deviations result from the abnormally large values of $<\tau_\beta>$ at low q, which we ascribe to artifacts of the excess SANS (elastic) intensity arising from Bragg scattering from the spatially periodic G_I LLC structure. Nonetheless, linear least-squares regressions of q^2 *versus* $1/<\tau_\beta>$ over

the range 0.3 Å^{-1} ≤ q ≤ 1.1 Å^{-1} yielded excellent fits with $R^2 > 0.95$ at $w_0 = 6$ (G_I; Figure 5A) and $w_0 = 15$ (H_I; Figure 5B) that affirm the validity of these analyses and enable determination of $\langle D \rangle$ from the slopes of these plots (see also Tables S1-2). The noted q^2-dependence of these plots coupled with the limiting observation that $\langle \tau_\beta \rangle \rightarrow 0$ ps^{-1} as $q \rightarrow 0$ Å^{-1} strongly implies that we are measuring unrestricted diffusion in the LLC systems over the length- and time-scales probed by the QENS measurements. This notion is consistent with the linear time evolution of the water center-of-mass mean-square displacement (MSD) reported in complementary MD simulations of these systems over a 300 ns trajectory.[34] By performing multiple global fits of the QENS spectra using different initial input values and calculating the relative standard deviation of the resulting self-diffusion coefficients given in Table 1, we estimate a fitting error of ±10%. We also obtain slightly different results for $\langle D \rangle$, if we allow the background scaling parameter, b_w, to vary with q (Eq. 1) as opposed to treating it as a q-independent variable (Eq. 2) in our global fit. While most of the $\langle D \rangle$ values obtained via these different fitting approaches fall within the stated ±10% uncertainty, the $\langle D \rangle$ values for **Na-74d** and **K-74d** at $w_0 = 15$ differ by 19% and 15%, respectively. In view of this estimated QENS data fitting error and the systematic errors previously estimated from MD simulations,[41] we focus our discussion on qualitative trends in water dynamics as functions of surfactant counterion and hydration. We note that the remarkable consistency of the following qualitative trends and those uncovered in independently-derived, complementary MD simulations of these same LLC systems[34] support the validity of the above analysis.

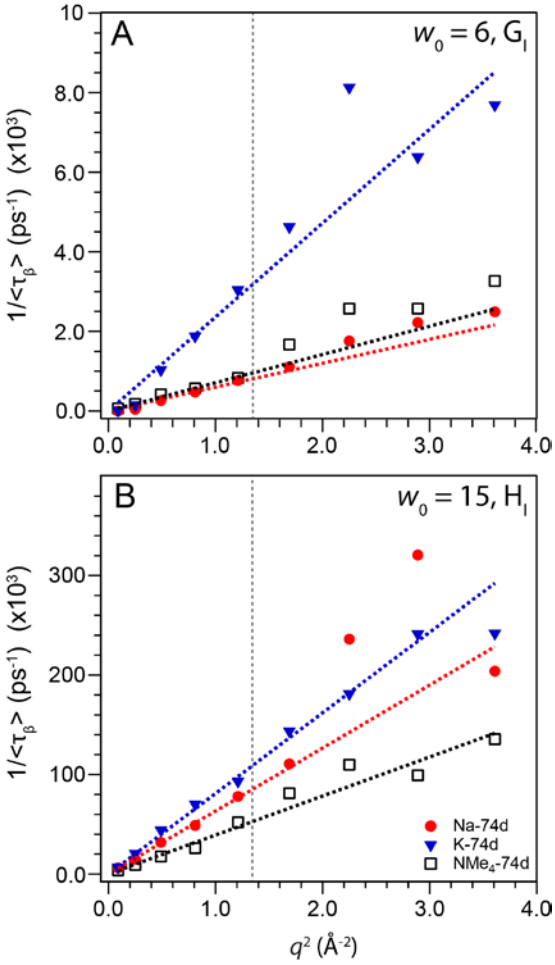

Figure 5. The water self-diffusion coefficient <*D*> was determined from the slope of $1/<\tau_\beta>$ *versus* q^2 plots, using a linear least-squares regression (*dashed lines*) over the range q = 0.3-1.1 Å^{-1} (*vertical dashed line*), where translational and rotational motions are sufficiently decoupled. Water diffusivity decreases in the order $K^+ > NMe_4^+ > Na^+$ for w_0 = 6 (**A**), and the order changes to $K^+ > Na^+ > NMe_4^+$ when w_0 = 15 (**B**).

Table 1. Dependence of Nanoconfined LLC Water Self-Diffusion Coefficients on Hydration and Counterion

Surfactant	Hydration	Morphology[a]	Nanopore Diameter (Å)[b]	$\langle D \rangle$ (cm^2/s)[c] (x 10^6) Eq. (1)	$\langle D \rangle$ (cm^2/s)[c] (x 10^6) Eq. (2)	$D_{Bulk}/\langle D \rangle$[d]
Na-74d	$w_0 = 6$	G_I	13	0.61 ± 0.06	0.65 ± 0.07	38
Na-74d	$w_0 = 15$	H_I	20	6.4 ± 0.6	5.2 ± 0.5	3.6
K-74d	$w_0 = 6$	G_I	13	2.4 ± 0.2	2.1 ± 0.2	9.7
K-74d	$w_0 = 15$	H_I	20	8.4 ± 0.8	7.2 ± 0.7	2.7
NMe_4-74d	$w_0 = 6$	G_I	15	0.69 ± 0.07	0.72 ± 0.07	33
NMe_4-74d	$w_0 = 15$	H_I	23	3.8 ± 0.4	4.0 ± 0.4	6.0
Na-AOT[48]	$w_0 = 3$	RM	14	2.80		8.6
Na-AOT[16]	$w_0 = 5$	RM	30.8	5		4.6

[a] Morphologies determined by synchrotron SAXS (see Figure 2). [b] Water nanopore diameters were estimated using electron density reconstructions (90% isosurface; see text for details). [c] Water self-diffusion constant determined from Figure 5, which derive from global fits of QENS spectra to either Eq (1) or Eq. (2). [d] Confinement-induced change in water dynamics determined by Eq. (1) as compared to $D_{Bulk} = 2.299 \times 10^{-5}$ cm^2/s for bulk water.[49, 50]

$\langle D \rangle$ strongly depends on both the surfactant counterion and the overall LLC hydration state, w_0. In the H_I phase at $w_0 = 15$, water diffusion between the lipidic cylinders slows modestly relative to bulk water:[49, 50]

$w_0 = 15$	**K-74d**	**Na-74d**	**NMe_4-74d**
$D_{Bulk}/\langle D \rangle$	2.7	3.6	6.0

As hydration decreases to $w_0 = 6$ in the G_I phase, water diffusion in the labyrinthine pores slows significantly with a different counterion-dependent trend:

$w_0 = 6$	**K-74d**	**NMe_4-74d**	**Na-74d**
$D_{Bulk}/\langle D \rangle$	9.7	33	38

To further explore the differences in water confined in **Na-74d** and **NMe_4-74d**, we conducted elastic intensity scans from 50–298 K. These experiments were performed on cooling to minimize disruption of the LLC phase by water crystallization and breakout from the soft lipidic nanoconfinement. From these data, we obtained the hydrogen atom mean-squared displacement (MSD) as a function of temperature ($\langle u^2_{X,H}(T)\rangle$) (Figure 6).[38] Values were normalized by assuming all diffusive motion ceased and the amplitude of harmonic vibration is minimal at 50 K ($\langle u^2_{X,H}(50\ K)\rangle = 0$). We obtain physically reasonable values for the H-atom MSD in each case: $\langle u^2_{X,H}\rangle = 0.17$ Å^2 for **Na-74d** at $w_0 = 6$ and $\langle u^2_{X,H}\rangle = 0.23$ Å^2 at $w_0 = 15$ at 298 K. For **NMe_4-74d** at $w_0 = 6$, $\langle u^2_{X,H}\rangle = 0.13$ Å^2. These observed H-atom MSDs at 298 K are slightly larger than those of 0.06–0.14 Å^2 observed for water confined within mesoporous silicas with ~2–3 nm diameter pores[51, 52] and those of 0.12 Å^2 observed for water confined in polyoxometallate cages.[38] However, the observed MSDs are smaller than that observed for bulk water.[53] Takahara *et al*. noted that the MSD in functionalized silica pores decreases with decreasing pore size,[51] consistent with the observed trend in **Na-74d** from $w_0 = 15$ to $w_0 = 6$. Franks *et al*.[54] similarly observed that the H-atom MSD in aqueous solutions of $(CH_3)_3COH$ (*t*BuOH) decreases as the *t*BuOH concentration increases (tighter confinement). The fact that the MSD in the G_I phases is greater for water in **Na-74d** than **NMe_4-74d** at 298 K likely reflects the increased volume excluded by the physically larger NMe_4^+ counterions.

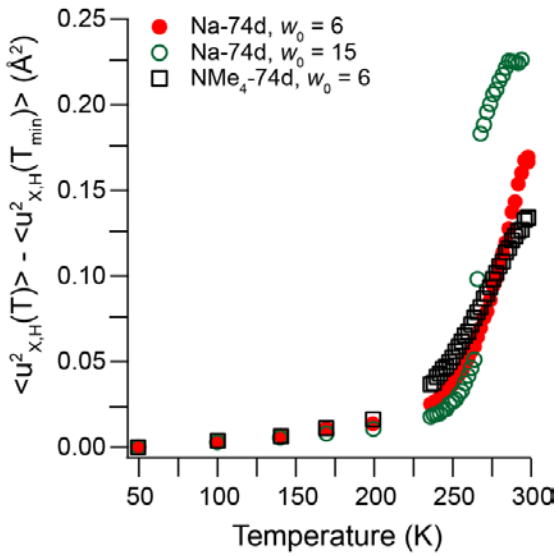

Figure 6. Both hydration and counterion identity influence the observed temperature-dependent H-atom MSDs of LLCs of **Na-74d** at w_0 = 6 (*red)* and w_0 = 15 (*green*), and the **NMe_4-74d** LLC at w_0 = 6 (*black*). At 298 K and w_0 = 6, the MSD in the **NMe_4-74d** sample is lower than that of **Na-74d**, due to the greater excluded volume of the larger counterion. The H-atom MSD is larger at the higher hydration for **Na-74d** LLCs at temperatures above the onset of water crystallization for the w_0 = 15 sample near 265 K (see text for details).

When $T <$ 275 K, the order reverses such that the MSD is higher in **NMe_4-74d** at lower temperatures. This crossover may stem from differences in the temperature-dependent solvation of the softer and more hydrophobic NMe_4^+ ion as compared to the hydrophilic Na^+ ion. Similar effects have been noted in aqueous solutions of NMe_4Br[55] and with other hydrophobic solutes such as tetramethylurea (TMU) and trimethylamine *N*-oxide (TMAO),[56] whereby water rotational dynamics accelerate relative to bulk water below a threshold temperature. The MSD gradually decreases with temperature for both samples at w_0 = 6, signifying a shrinking fraction of mobile ^{1}H atoms. Similar behavior has been noted in the hydration-dependent behavior of water confined between lipid bilayers,[17] indicating that water confined in the LLC gyroid nanopores behaves as if it is a supercooled liquid at temperatures as low as 50 K. In contrast, we

observe a sharp decrease in the MSD at ~265 K for **Na-74d** at w_0 = 15. Physically, this observation indicates that the H-atom vibrational amplitudes sharply decrease over a narrow temperature range, as expected for water crystallizing into ice. Previous studies of bulk water[57] and water confined between lipid bilayers[58, 59] reported similarly sharp discontinuities in the elastic intensity (related to the MSD) that were assigned to bulk-like water crystallization. Due to the non-covalent nature of the self-assembled LLCs, bulk water crystallization at the higher hydration w_0 = 15 may occur by disruption of the supramolecular morphology.

DISCUSSION

In electrolyte solutions, the observed water dynamics depend on both counterion-water attractions and counterion excluded volume. Since the strength of the counterion-water attractions depends on the charge densities of the ions,[31, 34, 60] the water self-diffusion coefficients should decrease in the order $NMe_4^+ > K^+ > Na^+$. On the other hand, the physical size of the counterion embodied in its excluded volume leads to slower water dynamics by sterically impeding the approach of new hydrogen bonding partners.[60] Based on counterion excluded volume alone, one would expect water diffusivity in these aqueous electrolytes to decrease in the order $Na^+ > K^+ > NMe_4^+$. Experimental[61, 62] and MD simulation investigations[34] have shown that water diffusivity in aqueous MCl solutions actually decreases in a different order: $K^+ > Na^+ > NMe_4^+$. Thus, the large excluded volume of the NMe_4^+ ion outweighs its low charge density and cation-water attractions induce slower water diffusion for Na^+ than for the more polarizable K^+. Furthermore, more recent MD simulations reveal that water diffusion for MCl solutions exhibits the same counterion-dependent trend at w_0 = 6 as at w_0 = 15.[34] These results demonstrate that the

relative contributions of counterion excluded volume and counterion-water attractions remain constant over this hydration range in homogenous aqueous electrolytes.

QENS measurements of water dynamics in gemini dicarboxylate LLCs divulge significant perturbations in water diffusivity within the carboxylate-lined sub-2.5 nm pores. The low β– values from KWW fits indicate that water dynamics are increasingly heterogeneous at low hydrations. In agreement with previous experimental studies of confined water,[63, 64] the magnitudes of the water self-diffusion coefficients in LLCs markedly differ from those observed in aqueous ionic solutions. Brown *et al*. demonstrated that QENS and ^{1}H NMR yield similar water diffusion coefficients for concentrated NMe_4Cl solutions.[61] At high hydrations of w_0 = 15 (~ 3.7 *m* salt in H_2O), $\langle D_{H_2O,MCl} \rangle$ measured by NMR in aqueous monovalent electrolyte solutions of NaCl, KCl, or NMe_4Cl is similar to that of bulk water, presumably due to the relatively low ion concentration. However, $\langle D_{H_2O,MCl} \rangle$ within those aqueous electrolytes is still faster than that in water confined in H_I LLCs with w_0 = 15 by factors of 3, 3, and 5, respectively.[61, 62] The magnitude of this divergence increases with LLC pore diameter reduction: water diffusion in NMe_4Cl at w_0 = 4.5 is 10 times faster than in the **NMe_4-74d** G_I LLC at w_0 = 6. While NaCl and KCl are insoluble in water at hydrations comparable to our QENS experiments, MD simulations of such solutions at w_0 = 6 confirm this trend.[34]

The present experiments and recent companion MD simulations[34] of water confined within the convex nanopores of gemini dicarboxylate LLCs demonstrate that its dynamics depend on counterion-water attractions and counterion excluded volume (Figure 7). In LLCs at w_0 = 15, we observe $\langle D_{H_2O,K^+} \rangle > \langle D_{H_2O,Na^+} \rangle > \langle D_{H_2O,NMe_4^+} \rangle$ (Table 1). This counterion-dependent trend is exactly that reported for bulk electrolyte solutions,[61, 65] supporting the idea that both counterion-water attractions and counterion excluded volume influence confined water diffusion. Since the

difference in excluded volume between Na^+ and K^+ is negligible,[34] we reason that the higher charge density of Na^+ drives increased counterion-water attractions that slow water diffusion in **Na-74d** LLCs (Figure 7A). On the other hand, the large and polarizable NMe_4^+ ion occupies a large fraction of the aqueous channel volume and sterically slows water diffusion (Figure 7B). This microscopic trend in the excluded volume is consistent with the observed decrease in the MSD at 298 K between **Na-74d** and **NMe_4-74d** shown in Figure 6, as well as the changes in the water volume fraction documented in complementary MD simulations.[34]

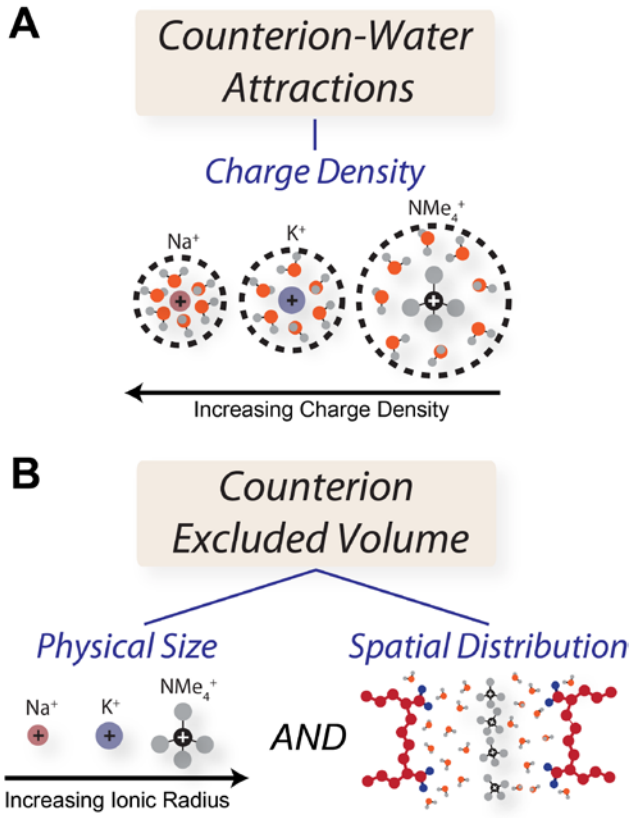

Figure 7. Counterion-water attractions and counterion excluded volume result in slower water dynamics. (**A**) The increased charge density of smaller ions results in stronger counterion-water attractions which slow water diffusion. (**B**) While counterion excluded volume depends only on the physical size of the counterion in concentrated electrolyte solutions, counterion excluded volume in ionic nanopores depends on both the ion size *and* their spatial distribution.

Unlike previous studies of electrolyte solutions and of water confined within **AOT** RMs,[64, 66] we observe a counterion-dependent trend in water diffusion that depends on LLC hydration.

Unexpectedly, we observe $\langle D_{H_2O,K^+} \rangle > \langle D_{H_2O,NMe_4^+} \rangle > \langle D_{H_2O,Na^+} \rangle$ at $w_0 = 6$. While MD simulations of these systems attributed this crossover in counterion-dependent water dynamics to the heightened importance of counterion-water attractions at low hydrations,[34] this reasoning fails to explain why water diffusion in LLCs differs from concentrated salt solutions. Previous studies by Levinger and co-workers of nanoconfined water dynamics in concave **AOT** RMs demonstrated the principal role of counterion-water attractions, as water dynamics primarily correlate with the counterion charge densities (Ca^{2+}, Na^+, K^+, and NH_4^+) over the hydration range w_0 = 1.1–5.0.[64, 67, 68] While subsequent MD simulations of **AOT** RMs with Na^+, K^+, or Cs^+ counterions affirmed this trend at $w_0 = 5$, Ladanyi and co-workers also argued that **AOT** RM water dynamics are also affected by differences in the spatial distribution of the counterions.[66]

The high-resolution synchrotron SAXS data presented in Figure 2 provide opportunities to directly assess the counterion distributions in the aqueous nanochannels of gemini surfactant LLCs, by reconstruction of real-space electron density maps. Following an established methodology,[69-72] we used the *JANA2006* software package[73] to conduct a Le Bail refinement of the SAXS patterns in Figure 2 in order to extract the structure factor intensities for each observed SAXS peak. Using these Fourier amplitudes as inputs for the "charge-flipping" algorithm *SUPERFLIP*, we reconstructed an electron density map for each studied LLC morphology (see Supporting Information and Table S3 for details).[74] Electron density maps of the G_I phase (90% isosurface) reveal the expected pair of interpenetrating networks of 3-fold lipidic connectors nested in a water matrix (Figure 8A). Although the local nanopore diameter varies slightly throughout this morphology,[75] we define the aqueous channel diameter for the G_I network as the distance between adjacent hydrophobic cables along the [111] direction. We estimate that the convex pore confinement diameter in the G_I LLC is $d \sim 13$ Å; similar analyses for H_I phase e^-

density maps (Figure S2) indicate water nanopores with $d \sim 20$ Å along [11] direction (Table 1). Further inspection of the electron densities in the (110) plane (Figure 8B) and 1D e^- density profiles along [111] direction in that plane (Figure 8C) reveal pronounced differences between the **NMe_4-74d** G_I phase and the **Na-74d** or **K-74d** analogs. The **NMe_4-74d** G_I phase exhibits depressed e^- density at the centers of the aqueous nanochannels with a width of ~ 6 Å, which we ascribe to the spatial localization of the NMe_4^+ counterions near the center of the G_I nanopores (Figure 8D). In contrast, the linear e^- density profiles for the **Na-74d** and **K-74d** G_I phases along the [111] direction in the (110) plane vary smoothly from the hydrophobic cable surface to the aqueous channel center, implying a more uniform distribution of the inorganic counterions in the nanopores (Figure 8D). Notably, we observe no sign of counterion localization in the H_I phase electron density maps of any of these systems (Figure S2).

Previous neutron diffraction studies[76,77] did not find any signature for NMe_4^+ ion localization in concentrated $NMe_4Cl(aq)$ solutions, in contrast to that in the pores of **NMe_4-74d** G_I LLCs (Figure 8). Ion localization decreases the excluded volume of NMe_4^+ and results in faster than expected H_2O dynamics for the **NMe_4-74d** LLC. In contrast, we find no evidence for alkali cation localization within the G_I nanochannels, presumably due to the strong electrostatic repulsions between the highly correlated, point-like charges.[78]

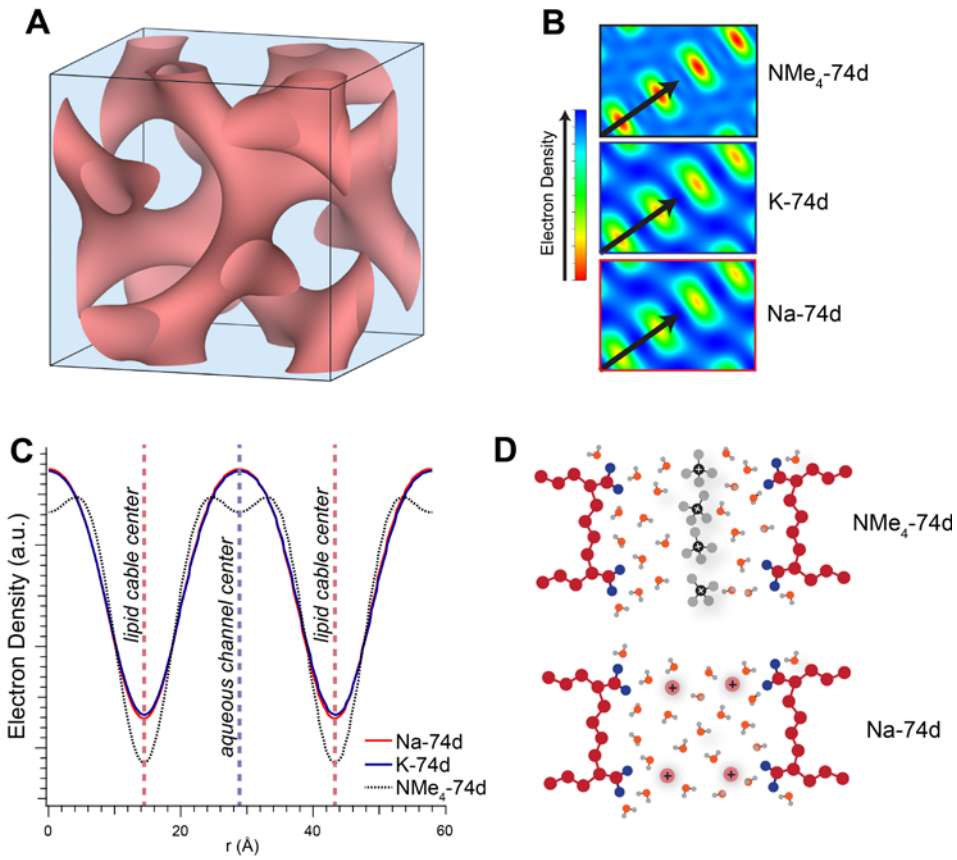

Figure 8 (**A**) G_I phase electron density map (90% isosurface) derived from SAXS data for the **Na-74d** LLC at w_0 = 6, from which the distance between lipidic cables (pink) along the [111] direction was used to estimate the aqueous nanochannel diameter. (**B**) 2D electron density maps (*absolute scale*) of the (110) plane of the G_I phase, where regions of lower electron density (*red*) correspond to the hydrophobic cables and regions of higher electron density (*blue*) correspond to the water and counterions. (**C**) Linear electron density profile along the [111] direction in the (110) plane (*black arrows in B*). The depleted electron density at the center of the aqueous channel of the **NMe_4-74d** LLC indicates NMe_4^+ counterion localization at the nanochannel center, while the smooth electron density profiles for **Na-74d** and **K-74d** LLCs indicate a more homogeneous distribution of the inorganic counterions therein. (**D**) Schematic depiction of the counterion distributions in the aqueous channels of **NMe_4-74d** and **Na-74d** LLCs contrasting the highly localized NMe_4^+ ions (*black*) to the more homogeneously distributed Na^+ ions (*red*).

The observation $\langle D_{H_2O,NMe_4^+} \rangle > \langle D_{H_2O,Na^+} \rangle$ is especially surprising given the changes in the magnitude of the interactions between water and the $-CO_2^-$ headgroups, which depend on the extent of surfactant headgroup–counterion pairing. Dilute micellar solution measurements[79]

indicate that cation association with alkyl carboxylate headgroups increases in the order NMe_4^+ < K^+ < Na^+. Thus, headgroup-water attractions are the strongest for NMe_4^+ and the weakest for Na^+. In spite of these changes in headgroup-water attractive interactions, ion localization apparently decreases the volume excluded by NMe_4^+ ions enough, so that the water attractions to the more homogeneously-distributed Na^+ ions dominate the water diffusion. Unlike in concentrated salt solutions, counterion excluded volume in an ionic nanopore thus depends not only on the physical size of the counterions, but also on their spatial distribution (Figure 7B).

Within LLC nanopores lined with ionic functionalities, pore interfacial curvature also apparently influences water dynamics. The data presented in Table 1 reveals that water diffusion is significantly slower within the convex pores of **Na-74d** LLCs than in the concave pores of **Na-AOT** RMs. Water diffusion within the 13 Å diameter pores of the **Na-74d** G_I LLC at w_0 = 6 displays $D_{Bulk}/\langle D \rangle$ = 38. However, **Na-AOT** RMs with a similar 14 Å confinement diameter at w_0 = 3 exhibit $D_{Bulk}/\langle D \rangle$ = 8.6,[48] while those of a similar hydration of w_0 = 5 exhibit $D_{Bulk}/\langle D \rangle$ = 4.6.[16] In work by Spehr *et al.*,[48] the width of the Lorentzian representing water translational dynamics approaches 0 μeV as $q \rightarrow 0$ $Å^{-1}$, indicating that water in the **Na-AOT** RMs is not "trapped" over the QENS measurement timescale. Part of the difference in water diffusion between **Na-AOT** RMs and **Na-74** LLCs may arise from the softer $–SO_3^-$ headgroup and its weaker water interactions, although this effect should be counterbalanced by a concomitant increase in the pore volume excluded by the large anionic headgroup. However, it is unlikely that these differences in pore chemical functionalities alone account for the large changes in water diffusion between **Na-74d** LLCs and **Na-AOT** RMs. Work by the groups of Szleifer and Grzybowski[80] and our group[23] demonstrate that the degree of ionization of interfacial functionalities depends sensitively on surface curvature. Concave interfaces place pore wall

functionalities in close proximity, favoring the formation of tightly bound ion pairs to mitigate intermolecular electrostatic repulsions between dissociated ions. This molecular picture is consistent with observations that counterion association increases as **Na-AOT** RM size decreases.[63] Convex interfaces allow increased levels of ion dissociation (Figure 1), which slows water diffusion by virtue of increased counterion-water attractions and counterion excluded volume effects. Additionally, tightly associated ion pairs at a concave interface may be expected to behave more like nonionic moieties, possibly explaining the observed insensitivity of water dynamics to the chemical nature of an RM interface.[15]

Differences in the water self-diffusion constants of **Na-74d** LLCs and **Na-AOT** RMs could also originate from differences in the interfacial functional group densities in each of these self-assembled systems. Assuming that a **Na-AOT** RM forms a perfect spherical water nanopool and using the RM dimensions from MD simulations by Harpham *et al*.,[66] we geometrically calculate that the sulfonate headgroups at $w_0 = 5$ are located ~8.4 Å apart. Analogously, using the RM dimensions from Harpham *et al*. at $w_0 = 2.5$, we estimate that the $-SO_3^-$ headgroups in **Na-AOT** at $w_0 = 3$ are separated by ~ 8.2 Å. From the unit cell dimensions and a geometric model for the G_I phase (see Table S4),[81] we estimate that the $-COO^-$ headgroups are situated ~7.2 Å apart for **Na-74d** at $w_0 = 6$. Thus, the increased density of interfacial headgroups may contribute to slowing the water diffusion within **Na-74d** LLCs. Ongoing studies focus on water dynamics in sulfonate-based LLCs to investigate the detailed effects of headgroup chemistry and interfacial curvature.

While the present study demonstrates that water translational dynamics are markedly slower in **Na-74d** LLCs than in **Na-AOT** RMs, recent combined experimental and theoretical 2D-FTIR studies revealed that water rotational dynamics are faster in the **Na-74** G_I phase ($w_0 = 6.5$) as

compared to a **Na-AOT** RM (w_0 = 2) at similar nanoconfinement diameters.[7] In MD simulations of carboxylate- and sulfonate-based LLCs at identical hydrations and convex pore interfacial curvatures, McDaniel *et al*.[18] observed *faster* rotational dynamics yet *slower* translational dynamics for water in sulfonate-based LLCs. In aggregate, these studies suggest that H_2O rotational dynamics are more affected by the intrinsic geometry of the confining interface as a result of "curvature-induced frustration,"[82] which favors *faster rotational dynamics* for convex interfaces. In contrast, water translational dynamics are more dependent on the degree of headgroup-counterion dissociation and the counterion distribution within the water-filled nanochannel, which depend on the geometry of the confining interface and favors *slower translational dynamics* for convex interfaces. These results also indicate that confined water resembles a supercooled liquid, wherein changes in rotational and translational dynamics may no longer be coupled.[83] Similar "glass–like" behavior has been noted in concentrated electrolyte solutions.[84] As noted in previously published MD simulations of the systems experimentally considered here,[85] rotation and translation are increasingly decoupled at low hydrations. Thus, a complete understanding of nanoconfined water dynamics requires separate quantification of rotational and translational dynamics.

CONCLUSION

QENS analyses of water nanoconfined in aqueous LLCs of dicarboxylate gemini surfactants demonstrate that translational H_2O dynamics sensitively depend on multiple features of the confining medium. Our experiments show that water dynamics depend principally on the hydration state of the system, in accord with MD simulations of water in these LLCs.[18] However, translational water dynamics also strongly depend on the identity of the surfactant counterions

and where they are situated in the aqueous nanochannels, due to the subtle competition between counterion-water attractions and counterion excluded volume. While the counterion excluded volume in concentrated salt solutions depends only on their physical size, we demonstrate that the counterion excluded volume in an ionic nanopore also depends on their spatial distribution. By comparing our results for water diffusivity within the convex pores of LLCs to those measured in the concave pores of AOT RMs, we demonstrate that pore interfacial curvature non-trivially influences nanoconfined water dynamics within a given system at similar hydrations and confinement diameters. These results also highlight the fact that translational and rotational dynamics may be decoupled in confined media, and thus care must be exercised in correlating these phenomena. In summary, hydration, interfacial curvature, and interfacial chemical functionalities are important variables that may be used to subtly manipulate nanoconfined water dynamics in various applications.

ASSOCIATED CONTENT

Supporting Information. Materials and methods, perdeuterated amphiphile synthesis and characterization, LLC sample preparation, SAXS analysis conditions, calculations of surfactant headgroup interfacial density, electron density reconstructions, representative QENS fitting parameters, and complete citation for reference 36. This material is available free of charge via the Internet at http://pubs.acs.org.

AUTHOR INFORMATION

Corresponding Author

*Email: maheshkm@umn.edu. Phone: +1-612-625-4599

Present Addresses

[§]Smiths Detection Inc., 2202 Lakeside Boulevard, Edgewood, MD 21040 USA

ORCID

Mahesh K. Mahanthappa: 0000-0002-9871-804X

Grayson L. Jackson: 0000-0003-0663-3274

Souleymane Omar-Diallo: 0000-0002-3369-8391

Arun Yethiraj: 0000-0002-8579-449X

Kenneth W. Herwig: 0000-0002-6798-2382

Sriteja Mantha: 0000-0001-7813-0903

Author Contributions

The manuscript was written through contributions of all authors. All authors have given approval to the final version of the manuscript.

Notes

The authors declare no competing financial interest.

ACKNOWLEDGMENT

We gratefully acknowledge financial support for this work from the U.S. Department of Energy Basic Energy Sciences (DOE BES) grant DE-SC0010328. GLJ acknowledges a National Defense Science and Engineering Graduate (NDSEG) Fellowship from the U.S. Department of Defense. Synchrotron SAXS analyses were conducted at Sector 12 of the Advanced Photon Source at Argonne National Laboratory, which is supported through the U.S. DOE Contract DE-

AC02-06CH11357 under GUP-48102 and GUP-42048. This research used resources at the Spallation Neutron Source, a DOE Office of Science User Facility operated by the Oak Ridge National Laboratory. We thank the Rick Goyette for logistical support during our BASIS measurement, Antonio Faraone for useful discussions regarding QENS data analysis, and Jose M. Borreguero for MANTID program support. This work also utilized University of Wisconsin-Madison instrumentation facilities funded in part by NSF CHE-9974839 and CHE-1048642, and materials characterization facilities funded by DMR-0832760 and DMR-1121288. Parts of this work were carried out in the Characterization Facility, University of Minnesota, which receives partial support from the University of Minnesota NSF MRSEC (DMR-1420013). Research reported in this publication was also supported by facilities funded by the Office of the Director, National Institutes of Health of the National Institutes of Health under Award Number S10OD011952. The content is solely the responsibility of the authors and does not necessarily represent the official views of the National Institutes of Health.

References

1. Fayer, M. D.; Levinger, N. E. Analysis of Water in Confined Geometries and at Interfaces. *Ann. Rev. Anal. Chem.* **2010,** *3*, 89-107.
2. Davis, J. G.; Gierszal, K. P.; Wang, P.; Ben-Amotz, D. Water Structural Transformation at Molecular Hydrophobic Interfaces. *Nature* **2012,** *491*, 582-585.
3. Soper, A. K. Radical Re-Appraisal of Water Structure in Hydrophilic Confinement. *Chem. Phys. Lett.* **2013,** *590*, 1-15.
4. Zhang, Y.; Faraone, A.; Kamitakahara, W. A.; Liu, K.-H.; Mou, C.-Y.; Leão, J. B.; Chang, S.; Chen, S.-H. Density Hysteresis of Heavy Water Confined in a Nanoporous Silica Matrix. *Proc. Natl. Acad. Sci. U. S. A.* **2011,** *108*, 12206-12211.
5. Hummer, G.; Rasaiah, J. C.; Noworyta, J. P. Water Conduction through the Hydrophobic Channel of a Carbon Nanotube. *Nature* **2001,** *414*, 188-190.
6. Kolesnikov, A. I.; Zanotti, J.-M.; Loong, C.-K.; Thiyagarajan, P.; Moravsky, A. P.; Loutfy, R. O.; Burnham, C. J. Anomalously Soft Dynamics of Water in a Nanotube: A Revelation of Nanoscale Confinement. *Phys. Rev. Lett.* **2004,** *93*, 035503.
7. Roy, S.; Skoff, D.; Perroni, D. V.; Mondal, J.; Yethiraj, A.; Mahanthappa, M. K.; Zanni, M. T.; Skinner, J. L. Water Dynamics in Gyroid Phases of Self-Assembled Gemini Surfactants. *J. Am. Chem. Soc.* **2016,** *138*, 2472-2475.
8. Raghavender, U. S.; Aravinda, S.; Shamala, N.; Kantharaju; Rai, R.; Balaram, P. Characterization of Water Wires inside Hydrophobic Tubular Peptide Structures. *J. Am. Chem. Soc.* **2009,** *131*, 15130-15132.
9. Duboué-Dijon, E.; Fogarty, A. C.; Hynes, J. T.; Laage, D. Dynamical Disorder in the DNA Hydration Shell. *J. Am. Chem. Soc.* **2016,** *138*, 7610-7620.
10. Grossman, M.; Born, B.; Heyden, M.; Tworowski, D.; Fields, G. B.; Sagi, I.; Havenith, M. Correlated Structural Kinetics and Retarded Solvent Dynamics at the Metalloprotease Active Site. *Nat. Struct. Mol. Biol.* **2011,** *18*, 1102-1108.
11. Stals, P. J. M.; Cheng, C.-Y.; van Beek, L.; Wauters, A. C.; Palmans, A. R. A.; Han, S.; Meijer, E. W. Surface Water Retardation around Single-Chain Polymeric Nanoparticles: Critical for Catalytic Function? *Chem. Sci.* **2016,** *7*, 2011-2015.
12. Hickner, M. A. Water-Mediated Transport in Ion-Containing Polymers. *J. Polym. Sci. Part B: Polym. Phys.* **2012,** *50*, 9-20.
13. Song, J.; Han, O. H.; Han, S. Nanometer-Scale Water- and Proton-Diffusion Heterogeneities across Water Channels in Polymer Electrolyte Membranes. *Angew. Chem. Int. Ed.* **2015,** *54*, 3615-3620.
14. Moilanen, D. E.; Fenn, E. E.; Wong, D.; Fayer, M. D. Geometry and Nanolength Scales Versus Interface Interactions: Water Dynamics in Aot Lamellar Structures and Reverse Micelles. *J. Am. Chem. Soc.* **2009,** *131*, 8318-8328.
15. Moilanen, D. E.; Levinger, N. E.; Spry, D. B.; Fayer, M. D. Confinement or the Nature of the Interface? Dynamics of Nanoscopic Water. *J. Am. Chem. Soc.* **2007,** *129*, 14311-14318.
16. Harpham, M. R.; Ladanyi, B. M.; Levinger, N. E.; Herwig, K. W. Water Motion in Reverse Micelles Studied by Quasielastic Neutron Scattering and Molecular Dynamics Simulations. *J. Chem. Phys.* **2004,** *121*, 7855-7868.
17. Miskowiec, A.; Buck, Z. N.; Hansen, F. Y.; Kaiser, H.; Taub, H.; Tyagi, M.; Diallo, S. O.; Mamontov, E.; Herwig, K. W. On the Structure and Dynamics of Water Associated with Single-Supported Zwitterionic and Anionic Membranes. *J. Chem. Phys.* **2017,** *146*, 125102.

18. McDaniel, J. G.; Mantha, S.; Yethiraj, A. Dynamics of Water in Gemini Surfactant-Based Lyotropic Liquid Crystals. *J. Phys. Chem. B* **2016,** *120*, 10860-10868.
19. Pizzitutti, F.; Marchi, M.; Sterpone, F.; Rossky, P. J. How Protein Surfaces Induce Anomalous Dynamics of Hydration Water. *J. Phys. Chem. B* **2007,** *111*, 7584-7590.
20. Fogarty, A. C.; Laage, D. Water Dynamics in Protein Hydration Shells: The Molecular Origins of the Dynamical Perturbation. *J. Phys. Chem. B* **2014,** *118*, 7715-7729.
21. Malardier-Jugroot, C.; Johnson, M. E.; Murarka, R. K.; Head-Gordon, T. Aqueous Peptides as Experimental Models for Hydration Water Dynamics near Protein Surfaces. *Phys. Chem. Chem. Phys.* **2008,** *10*, 4903-4908.
22. Russo, D.; Murarka, R. K.; Copley, J. R. D.; Head-Gordon, T. Molecular View of Water Dynamics near Model Peptides. *J. Phys. Chem. B* **2005,** *109*, 12966-12975.
23. Jackson, G. L.; Perroni, D. V.; Mahanthappa, M. K. Roles of Chemical Functionality and Pore Curvature in the Design of Nanoporous Proton Conductors. *J. Phys. Chem. B* **2017,** *121*, 9429-9436.
24. Berrod, Q.; Lyonnard, S.; Guillermo, A.; Ollivier, J.; Frick, B.; Manseri, A.; Améduri, B.; Gébel, G. Nanostructure and Transport Properties of Proton Conducting Self-Assembled Perfluorinated Surfactants: A Bottom-up Approach toward Pfsa Fuel Cell Membranes. *Macromolecules* **2015,** *48*, 6166-6176.
25. Hanot, S.; Lyonnard, S.; Mossa, S. Water Confined in Self-Assembled Ionic Surfactant Nano-Structures. *Soft Matter* **2015,** *11*, 2469-2478.
26. Gin, D. L.; Bara, J. E.; Noble, R. D.; Elliott, B. J. Polymerized Lyotropic Liquid Crystal Assemblies for Membrane Applications. *Macromol. Rapid. Commun.* **2008,** *29*, 367-389.
27. Zhou, M.; Nemade, P. R.; Lu, X.; Zeng, X.; Hatakeyama, E. S.; Noble, R. D.; Gin, D. L. New Type of Membrane Material for Water Desalination Based on a Cross-Linked Bicontinuous Cubic Lyotropic Liquid Crystal Assembly. *J. Am. Chem. Soc.* **2007,** *129*, 9574-9575.
28. Pindzola, B. A.; Jin, J.; Gin, D. L. Cross-Linked Normal Hexagonal and Bicontinuous Cubic Assemblies Via Polymerizable Gemini Amphiphiles. *J. Am. Chem. Soc.* **2003,** *125*, 2940-2949.
29. Sorenson, G. P.; Coppage, K. L.; Mahanthappa, M. K. Unusually Stable Aqueous Lyotropic Gyroid Phases from Gemini Dicarboxylate Surfactants. *J. Am. Chem. Soc.* **2011,** *133*, 14928-14931.
30. Perroni, D. V.; Baez-Cotto, C. M.; Sorenson, G. P.; Mahanthappa, M. K. Linker Length-Dependent Control of Gemini Surfactant Aqueous Lyotropic Gyroid Phase Stability. *J. Phys. Chem. Lett.* **2015,** *6*, 993-998.
31. Collins, K. D. Charge Density-Dependent Strength of Hydration and Biological Structure. *Biophys. J.* **1997,** *72*, 65-76.
32. Vlachy, N.; Jagoda-Cwiklik, B.; Vácha, R.; Touraud, D.; Jungwirth, P.; Kunz, W. Hofmeister Series and Specific Interactions of Charged Headgroups with Aqueous Ions. *Adv. Colloid Interfac.* **2009,** *146*, 42-47.
33. Jagoda-Cwiklik, B.; Vácha, R.; Lund, M.; Srebro, M.; Jungwirth, P. Ion Pairing as a Possible Clue for Discriminating between Sodium and Potassium in Biological and Other Complex Environments. *J. Phys. Chem. B* **2007,** *111*, 14077-14079.
34. Mantha, S.; Jackson, G. L.; Mahanthappa, M. K.; Yethiraj, A. Counterion-Regulated Dynamics of Water Confined in Lyotropic Liquid Crystalline Morphologies. *J. Phys. Chem. B* **2018,** *122*, 2408-2413.

35. Heiney, P. Datasqueeze Software. http://www.physics.upenn.edu/~heiney/datasqueeze/index.html (accessed September 21, 2018).
36. Taylor, J., Arnold, O.; Bilheaux, J.; Buts, A.; Campbell, S.; Doucet, M.; Draper, N.; Fowler, R.; Gigg, M.; Lynch, V. et al. Mantid, a High Performance Framework for Reduction and Analysis of Neutron Scattering Data. *Bull. Amer. Phys. Soc.* **2012,** *57*.
37. Mantid: Manipulation and Analysis Toolkit for Instrument Data. http://dx.doi.org/10.5286/softwarre/mantid (accessed September 21, 2018).
38. Faraone, A.; Fratini, E.; Todea, A. M.; Krebs, B.; Müller, A.; Baglioni, P. Dynamics of Water in Voids between Well-Defined and Densely Packed Spherical Nanocages Acting as Polyprotic Inorganic Acids. *J. Phys. Chem. C* **2009,** *113*, 8635-8644.
39. Faraone, A.; Liu, L.; Mou, C.-Y.; Shih, P.-C.; Copley, J. R. D.; Chen, S.-H. Translational and Rotational Dynamics of Water in Mesoporous Silica Materials: Mcm-41-S and Mcm-48-S. *J. Chem. Phys.* **2003,** *119*, 3963-3971.
40. Berrod, Q.; Lyonnard, S.; Guillermo, A.; Ollivier, J.; Frick, B.; Gébel, G. Qens Investigation of Proton Confined Motions in Hydrated Perfluorinated Sulfonic Membranes and Self-Assembled Surfactants. *EPJ Web of Conferences* **2015,** *83*, 02002.
41. Mantha, S.; Yethiraj, A. Dynamics of Water Confined in Lyotropic Liquid Crystals: Molecular Dynamics Simulations of the Dynamic Structure Factor. *J. Chem. Phys.* **2016,** *144*, 084504.
42. Chen, S. H.; Liao, C.; Sciortino, F.; Gallo, P.; Tartaglia, P. Model for Single-Particle Dynamics in Supercooled Water. *Phys. Rev. E* **1999,** *59*, 6708-6714.
43. Faraone, A.; Liu, L.; Chen, S.-H. Model for the Translation–Rotation Coupling of Molecular Motion in Water. *J. Chem. Phys.* **2003,** *119*, 6302-6313.
44. Faraone, A.; Liu, K.-H.; Mou, C.-Y.; Zhang, Y.; Chen, S.-H. Single Particle Dynamics of Water Confined in a Hydrophobically Modified Mcm-41-S Nanoporous Matrix. *J. Chem. Phys.* **2009,** *130*, 134512.
45. Zanotti, J. M.; Bellissent-Funel, M. C.; Chen, S. H. Relaxational Dynamics of Supercooled Water in Porous Glass. *Phys. Rev. E* **1999,** *59*, 3084-3093.
46. Chen, S. H.; Gallo, P.; Sciortino, F.; Tartaglia, P. Molecular-Dynamics Study of Incoherent Quasielastic Neutron-Scattering Spectra of Supercooled Water. *Phys. Rev. E* **1997,** *56*, 4231-4243.
47. Liu, L.; Faraone, A.; Chen, S.-H. Model for the Rotational Contribution to Quasielastic Neutron Scattering Spectra from Supercooled Water. *Phys. Rev. E* **2002,** *65*, 041506.
48. Spehr, T. L.; Frick, B.; Zamponi, M.; Stuhn, B. Dynamics of Water Confined to Reverse Aot Micelles. *Soft Matter* **2011,** *7*, 5745-5755.
49. Mills, R. Self-Diffusion in Normal and Heavy Water in the Range 1-45 Degrees. *J. Phys. Chem.* **1973,** *77*, 685-688.
50. Holz, M.; Heil, S. R.; Sacco, A. Temperature-Dependent Self-Diffusion Coefficients of Water and Six Selected Molecular Liquids for Calibration in Accurate 1h Nmr Pfg Measurements. *Phys. Chem. Chem. Phys.* **2000,** *2*, 4740-4742.
51. Takahara, S.; Sumiyama, N.; Kittaka, S.; Yamaguchi, T.; Bellissent-Funel, M.-C. Neutron Scattering Study on Dynamics of Water Molecules in Mcm-41. 2. Determination of Translational Diffusion Coefficient. *J. Phys. Chem. B* **2005,** *109*, 11231-11239.
52. Briman, I. M.; Rébiscoul, D.; Diat, O.; Zanotti, J.-M.; Jollivet, P.; Barboux, P.; Gin, S. Impact of Pore Size and Pore Surface Composition on the Dynamics of Confined Water in Highly Ordered Porous Silica. *J. Phys. Chem. C* **2012,** *116*, 7021-7028.

53. Teixeira, J.; Bellissent-Funel, M. C.; Chen, S. H.; Dianoux, A. J. Experimental Determination of the Nature of Diffusive Motions of Water Molecules at Low Temperatures. *Phys. Rev. A* **1985,** *31*, 1913-1917.
54. Franks, F. R., J.; Egelstaff, P. A.; Page, D. I. Motions of Water Molecules in Dilute Aqueous Solutions of Tertiary Butyl Alcohol; a Neutron Scattering Study of Hydrophobic Hydration. *P. Roy. Soc. A-Math. Phy.* **1970,** *319*, 189-208.
55. Bradl, S.; Lang, E. W. Hydration Water Dynamics in Undercooled Aqueous Solutions of Hydrophobic Ions. *J. Phys. Chem.* **1993,** *97*, 10463-10471.
56. Qvist, J.; Halle, B. Thermal Signature of Hydrophobic Hydration Dynamics. *J. Am. Chem. Soc.* **2008,** *130*, 10345-10353.
57. Diallo, S. O.; Mamontov, E.; Nobuo, W.; Inagaki, S.; Fukushima, Y. Enhanced Translational Diffusion of Confined Water under Electric Field. *Phys. Rev. E* **2012,** *86*, 021506.
58. Rheinstädter, M. C.; Seydel, T.; Demmel, F.; Salditt, T. Molecular Motions in Lipid Bilayers Studied by the Neutron Backscattering Technique. *Phys. Rev. E* **2005,** *71*, 061908.
59. Swenson, J.; Kargl, F.; Berntsen, P.; Svanberg, C. Solvent and Lipid Dynamics of Hydrated Lipid Bilayers by Incoherent Quasielastic Neutron Scattering. *J. Chem. Phys.* **2008,** *129*, 045101.
60. Stirnemann, G.; Wernersson, E.; Jungwirth, P.; Laage, D. Mechanisms of Acceleration and Retardation of Water Dynamics by Ions. *J. Am. Chem. Soc.* **2013,** *135*, 11824-11831.
61. Brown, A. N.; Newbery, M.; Thomas, R. K.; White, J. W. Ion and Solvent Dynamics in Aqueous Tetramethylammonium Chloride Solutions. *J. Chem. Soc. Faraday Trans.* **1988,** *84*, 17-33.
62. Müller, K. J.; Hertz, H. G. A Parameter as an Indicator for Water–Water Association in Solutions of Strong Electrolytes. *J. Phys. Chem.* **1996,** *100*, 1256-1265.
63. Park, S.; Moilanen, D. E.; Fayer, M. D. Water Dynamics: The Effects of Ions and Nanoconfinement. *J. Phys. Chem. B* **2008,** *112*, 5279-5290.
64. Pant, D.; Riter, R. E.; Levinger, N. E. Influence of Restricted Environment and Ionic Interactions on Water Solvation Dynamics. *J. Chem. Phys.* **1998,** *109*, 9995-10003.
65. Impey, R. W.; Madden, P. A.; McDonald, I. R. Hydration and Mobility of Ions in Solution. *J. Phys. Chem.* **1983,** *87*, 5071-5083.
66. Harpham, M. R.; Ladanyi, B. M.; Levinger, N. E. The Effect of the Counterion on Water Mobility in Reverse Micelles Studied by Molecular Dynamics Simulations. *J. Phys. Chem. B* **2005,** *109*, 16891-16900.
67. Riter, R. E.; Undiks, E. P.; Levinger, N. E. Impact of Counterion on Water Motion in Aerosol Ot Reverse Micelles. *J. Am. Chem. Soc.* **1998,** *120*, 6062-6067.
68. Riter, R. E.; Willard, D. M.; Levinger, N. E. Water Immobilization at Surfactant Interfaces in Reverse Micelles. *J. Phys. Chem. B* **1998,** *102*, 2705-2714.
69. Jayaraman, A.; Mahanthappa, M. K. Counterion-Dependent Access to Low-Symmetry Lyotropic Sphere Packings of Ionic Surfactant Micelles. *Langmuir* **2018**.
70. Baez-Cotto, C. M.; Mahanthappa, M. K. Micellar Mimicry of Intermetallic C14 and C15 Laves Phases by Aqueous Lyotropic Self-Assembly. *ACS Nano* **2018,** *12*, 3226-3234.
71. Kim, S. A.; Jeong, K. J.; Yethiraj, A.; Mahanthappa, M. K. Low-Symmetry Sphere Packings of Simple Surfactant Micelles Induced by Ionic Sphericity. *Proc. Natl. Acad. Sci. U. S. A.* **2017,** *114*, 4072-4077.

72. Sorenson, G. P.; Schmitt, A. K.; Mahanthappa, M. K. Discovery of a Tetracontinuous, Aqueous Lyotropic Network Phase with Unusual 3d-Hexagonal Symmetry. *Soft Matter* **2014,** *10*, 8229-8235.
73. Petříček, V.; Dušek, M.; Palatinus, L. Crystallographic Computing System Jana2006: General Features. *Z. Krist.-Cryst. Mater.* **2014,** *229*, 345-352.
74. Palatinus, L.; Chapuis, G. Superflip - a Computer Program for the Solution of Crystal Structures by Charge Flipping in Arbitrary Dimensions. *J. Appl. Cryst.* **2007,** *40*, 786-790.
75. Assenza, S.; Mezzenga, R. Curvature and Bottlenecks Control Molecular Transport in Inverse Bicontinuous Cubic Phases. *J. Chem. Phys.* **2018,** *148*, 054902.
76. Soper, A. K.; Turner, J.; Finney, J. L. Solute-Solute Correlations in Aqueous Solutions of Tetramethylammonium Chloride. *Mol. Phys.* **1992,** *77*, 431-437.
77. Turner, J.; Soper, A. K.; Finney, J. L. Water Structure in Aqueous Solutions of Tetramethylammonium Chloride. *Mol. Phys.* **1992,** *77*, 411-429.
78. Jho, Y. S.; Kanduč, M.; Naji, A.; Podgornik, R.; Kim, M. W.; Pincus, P. A. Strong-Coupling Electrostatics in the Presence of Dielectric Inhomogeneities. *Phys. Rev. Lett.* **2008,** *101*, 188101.
79. Brun, T. S.; Hoiland, H.; Vikingstad, E. The Fraction of Associated Counterions and Singly Dispersed Amphiphiles in Micellar Systems from Ion Exchange Membrane Electrode Measurements. *J. Colloid Interf. Sci.* **1978,** *63*, 590-592.
80. Wang, D.; Nap, R. J.; Lagzi, I.; Kowalczyk, B.; Han, S.; Grzybowski, B. A.; Szleifer, I. How and Why Nanoparticle's Curvature Regulates the Apparent Pka of the Coating Ligands. *J. Am. Chem. Soc.* **2011,** *133*, 2192-2197.
81. Gulik, A.; Luzzati, V.; De Rosa, M.; Gambacorta, A. Structure and Polymorphism of Bipolar Isopranyl Ether Lipids from Archaebacteria. *J. Mol. Bio.* **1985,** *182*, 131-149.
82. Pieniazek, P. A.; Lin, Y.-S.; Chowdhary, J.; Ladanyi, B. M.; Skinner, J. L. Vibrational Spectroscopy and Dynamics of Water Confined inside Reverse Micelles. *J. Phys. Chem. B* **2009,** *113*, 15017-15028.
83. Cerveny, S.; Mallamace, F.; Swenson, J.; Vogel, M.; Xu, L. Confined Water as Model of Supercooled Water. *Chem. Rev.* **2016,** *116*, 7608-7625.
84. Turton, D. A.; Hunger, J.; Hefter, G.; Buchner, R.; Wynne, K. Glasslike Behavior in Aqueous Electrolyte Solutions. *J. Chem. Phys.* **2008,** *128*, 161102.
85. Mondal, J.; Mahanthappa, M.; Yethiraj, A. Self-Assembly of Gemini Surfactants: A Computer Simulation Study. *J. Phys. Chem. B* **2013,** *117*, 4254-4262.

TOC GRAPHIC

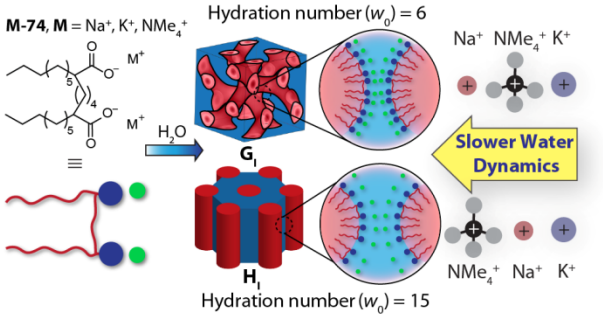
M-74, M = Na+, K+, NMe4+
M+
M+
H2O
Hydration number (w0) = 6
GI
HI
Hydration number (w0) = 15
Na+ NMe4+ K+
Slower Water Dynamics
NMe4+ Na+ K+